Towards a Dual-Tip STM Application in Mesoscopic Electron Transport

Rami Dana,[a,*] Irina Kiruschev,[b] Phong Dinh Tran,[c] Pascal Doppelt,[c] and Yishay Manassen[a]
[a]Department of Physics and the Ilse Katz Center for Nanoscience and Nanotechnology, P.O. Box 653, Ben-Gurion University of the Negev, Be'er Sheva 84105, Israel
[b]Irus Optomechanics LTD, Ha'Margnit 3, Ramat Gan 52584, Israel
[c]LIMHP, Université Paris 13, CNRS; Institut Galilée, 99 Avenue Jean-Baptiste Clément, 93430 Villetaneuse, France

(Received 1 February 2008 and in revised form 20 May 2008)

Abstract. A new design for a dual-tip scanning tunneling microscope (STM) is presented. The design is a variation on the mechanically controllable break-junction with two electron beam-induced deposition nano-tips. The new design enables one to scan surfaces simultaneously with two probes having a nano-gap separation. By collecting the lateral current flowing between the tips, the transconductance map can then be compared with the STM images for local characterizations of the electron transport. Since the lateral beam carries the property of the density of states of the surface at momentum space, the dispersion of the electronic structure should give an orientation and position dependence of the local transconductance current. In addition, the reduced terminal separation, on the order of the characteristic *mesoscopic* length scales, is likely to be sensitive to a variety of typically observed interactions and interference effects.

INTRODUCTION

The vertical current flowing between a single-tip scanning tunneling microscope (STM) and a surface can probe static properties of electronic systems such as local density of states. It has already been demonstrated[1,2] that a significant lateral surface component is also present. This lateral component carries an extremely fundamental property of the surface, namely, the electron density of states of the surface at momentum space (dispersion relations). In order to measure such local dispersion relations, one has to inject hot ballistic electrons with one electrode and collect them with a second electrode. As demonstrated by Angle Resolved UV Photoelectron Spectroscopy[3] (ARUPS), the two-dimensional momentum distributions at the surface are extremely anisotropic. Thus, If a lateral electron beam that traverses the surface between two biased electrodes can keep its direction and energy over distances of several nm (as indicated by Ballistic Electron Emission in 3D microscopy[4]), the dispersion of the electronic structure should give an orientation and position dependence of the local transconductance current. (However, for the electron to be ballistic, the probe separation must be very small.) The lateral component of the current can also display mesoscopic transport phenomena related to characteristic length scales and transport regimes, as will be discussed below. Some of these phenomena were verified by the fabrication of artificial structures that generate 3D down to 0D quantum entities. These patterns serve as fixed experimental setups with a predetermined and strongly coupled terminal contacts con-

*Author to whom correspondence should be addressed.
E-mail: ramid@bgu.ac.il

DOI 10.1560/IJC.48.2.87

figuration; thus, they lack the capability of performing local transport measurement on arbitrary systems and especially on surfaces. Transport on surfaces might be important since, as the conductor's dimensions become smaller, the surface-to-volume ratio becomes larger, and transport can be more surface-sensitive (as indicated by 4-probe measurements[5]).

Of all the different possible setups for multi-terminal experiments, the multi-probe STM (MPSTM) has the following benefits: self and changeable positioning of the leads with sub-nm precision, small (weakly coupled) point contact or tunneling mode measurements for high angular resolution, and its nature as a noninvasive technique. Indeed, in the last decade, various, but not many, attempts to construct an MPSTM were reported. In some of the attempts, atomic resolution of the probes was demonstrated; however, scientific results emerging from data collected by the MPSTM were only rarely followed up. In this paper we present a new approach for a dual-tip STM (DTSTM). Our design is based on the mechanically controllable break-junction (MCBJ) with two electron beam-induced deposition (EBID) nanotips. Integration of the special characteristics of these techniques leads to a DTSTM capable of less than 100-nm probe separation, as will be presented here. On these scales more local and less averaged information can be collected; thus, new insight on electron transport phenomena on the nanoscale will hopefully be gained. The nature of current flow on these scales can be interesting from both fundamental physics and device application points of views.

The paper is organized as follows. In the first section, the merit of DTSTM will be introduced. Here we shall give the basic theory, outline the scientific applications, and explain our "second thoughts" regarding the effect of mesoscopic phenomena on the DTSTM setup. In the second section we shall summarize some of the main theoretical and experimental results dealing with two-terminal mesoscopic transport. After a short introduction to some relevant characteristic length scales and transport regimes, we shall start with the zero temperature and bias limit, move on to finite temperature and bias, address the phenomenon of *localization*, and conclude with a few remarks on mesoscopic transport and DTSTM. We shall mostly follow in the footsteps of S. Data[6] in this section, except for the introduction, where we follow the definitions of Mello and Kumar.[7] In the next section we shall give a detailed review of our design for a DTSTM based on the MCBJ with two EBID nanotips. First, the current status in the field of MPSTM will be reviewed. Our modification of the MCBJ including a special anisotropic-etching silicon micro-bridge will then be presented. Following it, we introduce the growing field of EBID and its integration in our design. Our preliminary results are then given. These include the apparatus itself, the silicon break-junction, and the fabrication of two adjustable independent EBID nanotips. We conclude by emphasizing the potential of our DTSTM.

DTSTM MERIT

Basic Theory and Applications

The realization and applications of a DTSTM were first analyzed by Niu et al. in 1995.[8] Since all single-particle properties can be derived from the Green's function, they used it to describe the propagation of the electrons between the tips and to highlight some possible applications. For a three-terminal setup with the sample at a constant chemical potential μ_0 and the tips biased with μ_1 and μ_2, each junction conductance is defined by $\sigma_i = \partial I_i/\partial V_i$. Using the Tersoff and Hamann formalism, Niu and coworkers found:

$$\sigma_i = (e^2/h)\Gamma_i\rho(\mathbf{r}_i,\mu_i) \qquad (1)$$

where $\rho(\mathbf{r}_i,\mu_i)$ is the local density of states of the sample at the chemical potential of tip i and Γ_i describes tip–sample coupling and the density of states at the tip. For $\mu_1 > \mu_2$, coherent tunneling of electrons through the sample gives rise to a transconductance current component in tip 2 defined by $\sigma_{21} \equiv \partial I_2/\partial V_1$. By accounting for the transition rates using the Fermi golden rule and second-order transition-matrix elements, they evaluate σ_{21} to be:

$$\sigma_{21} = (e^2/h)\Gamma_1\Gamma_2|G(\mathbf{r}_1, \mathbf{r}_2; \varepsilon = \mu_1)|^2 \qquad (2)$$

where $G(\mathbf{r}_1, \mathbf{r}_2; \varepsilon)$ is the retarded Green's function of the sample for noninteracting electrons in zero temperature. The detection limit for the transconductance current was estimated to be four orders of magnitude smaller than the tunneling current, thus, 0.1–1 pA.

Niu et al. highlighted the following four applications for the DTSTM: (1) Ballistic transport and surface state band structure—for free electrons, σ_{21} is supposed to be isotropic and $1/r$ dependent, but, by introducing an approximated 2D Green's function for the electrons propagating on a crystalline surface with Bloch waves, modulation and overall orientation dependence of the transconductance were uncovered. (2) Phase shift from a surface defect—in the presence of defects, the superposition of interference effects gives rise to modulation of $|G|^2$ when the second tip moves around relative to the first. (3) Transition from ballistic transport to diffusive to localization. (4) Inelastic mean free path—since G decays on this length scale, the inelastic mean free path and its energy dependence can be deduced from the decay of σ_{21} with tip separation and bias, respectively.

Experimental Realization

As much as STM detects a local density of states (LDOS) that differs from the bulk band structure, the DTSTM might detect the local and anisotropic dispersion relations instead of the averaged ARUPS data. This first application suggested by Niu and coworkers[8] for the detection of surface state band structure assumes ballistic transport for noninteracting electrons in zero temperature. But, when we think of a real experimental setup, a few questions arise. (1) At what conditions can a DTSTM be regarded as a two-terminal ballistic conduction setup? (2) How can the surface resistance be distinct from the tunnel junction's resistance? (3) What will be different if the electrons do interact? (4) How will finite temperatures modify the zero limit assumption? The answers for these questions can be found in the more general two-terminal ballistic transport phenomenon, which was extensively studied (both theoretically and experimentally) in mesoscopic physics. Moreover, the other applications suggested for the DTSTM, including phase shift from a surface defect and transition from ballistic transport to diffusive to localization and the detection of inelastic mean free path, all involve regimes, length scales, and quantum phenomena characteristic to the field of mesoscopic transport. Actually, the definition of the DTSTM–surface system might not be trivial at all. On the one hand, the two terminals can be either two tunneling junctions, two point contacts, or one of each. On the other hand, the surface can be 3D down to quasi-1D conductor[1] and can also demonstrate orientation and periodic (atoms, unit cell, reconstruction, steps) dependence. Thus, a variety of physical phenomena can enter into the data collected by a DTSTM and these might not be easy or even possible to separate. Since our design is aiming for tip separation on the order of the typical mesoscopic length scales, we have to be prepared for the two-terminal conductance behavior arising from it to affect our experiment. In the next section we will review a partial collection of the mesoscopic effects that can be important for the understanding of the data collected by our DTSTM. These will include: length scales and transport regimes; two-terminal transport at zero and finite temperature and bias; and weak-localization corrections to the classical conductance and fluctuations.

MESOSCOPIC TWO-TERMINAL TRANSPORT

Characteristic Length Scales and Transport Regimes

The definition of *mesoscopic* transport was originally introduced by van Kampen in the context of statistical mechanics, where the finite size effect dominates the thermal behavior. But, microstructures are often called *mesoscopic* when the phase of a single-electron wavefunction (in the independent-particle approximation) remains coherent across the system. Coherent means that the phase-coherence length l_ϕ associated with processes that can change the environment exceeds the system size L. Various time scales and length scales define and characterize the different regimes of *mesoscopic* transport and the statistics of the associated fluctuations in different samples. A canonical example is a disordered degenerate metallic system at low temperatures. In this system the *elastic mean free path* l_e for elastic scattering from a random impurity potential and the *Fermi wavelength* $\lambda_F \equiv (2\pi/k_F)$ define the dimensionless disorder parameter $(1/k_F l_e)$ that measures the degree of randomness. The *inelastic mean free path* l_{in} due to scattering by phonons, other electrons, etc., defines the time scale on which the electron wave loses its phase coherence $\tau_{in} \equiv l_{in}/v_F$, where v_F is the Fermi speed ($v_F = \hbar k_F / m$). In general it must be replaced by the *dephasing time* $\tau_\phi \equiv l_\phi/v_F$ (l_ϕ being the *dephasing length*) inasmuch as all inelastic scatterings are not equally effective. The elastic mean free path together with the Fermi speed define the *diffusion constant* $D_e = (1/3)v_F l_e$ (3D) and together with the inelastic scattering time they define the *Thouless length* $L_T = (D_e\ l_{in}) \equiv [(1/3)\ l_{in}\ l_e]^{1/2}$. L_T is the typical distance through which the electron diffuses before losing its phase coherence. For a typical *mesoscopic* conductor at low temperatures, $l_e < L_T < l_{in}$. In terms of these length scales, three experimental regimes for coherent transport $(1/k_F l_e << 1)$ can be defined:

(a) *Ballistic* ($\lambda_F < L << l_e,\ l_{in}$)—The wave propagates through the sample without any elastic or phase breaking scattering. All the scattering is at the boundary; thus, large statistical fluctuations are expected if the wavelength or the conductor shape are changed.

(b) *Diffusive weak-localization regime* ($\lambda_F << l_e << L < L_T$) – Here the wave traverses the system coherently, scattering is sample specific, and the statistical fluctuations are not suppressed by self-averaging.

(c) *Macroscopic* ($\lambda_F << l_e << L_T << L$) – Here the sample effectively breaks up into *mesoscopic* subsamples of size L_T of the coherently diffusive type (b). But, since there is no phase coherence between the subsamples, the transport properties are averaged, leading to "Ohmic" behavior of the conductance G (determined entirely by the material conductivity σ and the division of cross-section by length).

The effect of two other important length scales, which will not be treated in this paper, are the *thermal* $l_T = (\hbar D_e\ k_B T)$ and the *magnetic* $l_m = (\hbar/eB)$.

Zero Temperature and Bias

The resistance of a low-dimensional conductor has

two corrections to the simple "ohmic" picture: a length-independent resistance associated with the contacts and discrete steps related to the transverse modes M across the conductor. For a perfectly ballistic conductor (electrons suffer no scattering inside the conductor), the transition from many transverse modes M in the lead to few in the conductor, gives rise to contact resistance G_c^{-1}, independent of the conductor's length L. In the zero temperature and bias limit, current only flows down the chemical potential in the energy range $\mu_1 > E > \mu_2$ that converges to a single energy channel around the Fermi energy E_F. Thus, by assuming a constant number of modes M in the above range and reflectionless contacts (electrons suffer no reflections escaping into the contacts), we get a finite value for the contact conductance G_c:

$$G_c = (2e^2/h)M \tag{3}$$

Hence, for $M = 1$, (1D conductor), we observe the maximum value of $G_c^{-1} \sim 12.9$ kΩ. The source for the finite conductance was clarified by Imry[9] after earlier notations by Engquist and Anderson.[10] Since the contact resistance is inversely proportional to the number of modes and M can be estimated to be equal to Integer[$W/(\lambda_f/2)$], the resistance is raised in discrete steps of $h/2e^2$ as the conductor width W is becoming larger. The above two-terminal contact resistance was observed experimentally, first for metals[11] in the late 1960s and then for semiconductors[12,13] in 1988. Different modes were observed, for example, by Topinka et al.[14]

A useful approach in describing mesoscopic transport is to express current in terms of the transmission probability T for electrons to traverse across the conductor. By relating the linear response conductance (eq 8) to the transmission probability, the Landauer formalism[15] defines the conductance G for a two-terminal conductor by:

$$G = (2e^2/h)MT \tag{4}$$

For $T = 1$ the conductor is ballistic and we are left with the contact resistance from eq 3. For $T \neq 1$ it is useful to calculate the actual conductor resistance from a four-terminal Hall-bridge configuration (to be explained). The overall resistance G^{-1} can then be introduced as the contact resistance in series with the actual device resistance $(h/2e^2M)(1–T)/T$:

$$G^{-1} = (h/2e^2M) + (h/2e^2M)(1 - T)/T \tag{5}$$

Finite Temperature and Bias

The Landauer formula (4) is simplified to zero temperature, single energy channel, and unidirectional current. Thus, when the leads are at a different electrochemical potential ($\mu_1 - \mu_2 = \Delta\mu$), we can simply define the current by:

$$I = G(\mu_1 - \mu_2)/|e| = (2e/h)T(E_F)M(E_F)\Delta\mu \tag{6}$$

But, for finite temperature, transport takes place through multiple energy channels μ_1 + few $k_BT > E > \mu_2$– few k_BT, each with a possible different $T(E)$ and $M(E)$. In addition, at any energy channel, current can now flow into the conductor from both leads, proportional to $M(E)$ and the Fermi distribution $f_i(E)$ at the lead. In equilibrium $T(E)M(E)$ is the same in each direction and the total current is expressed by:

$$I = (2e/h)\int T(E)M(E)[\, f_1(E) - f_2(E)]dE \tag{7}$$

For small deviations from equilibrium ($\mu_1 \approx \mu_2$), I is proportional to the applied bias and we get the non-zero temperature linear response formula:

$$G(E) = (2e^2/h)\int T(E)M(E)(-\,\partial f_0/\partial E)dE \tag{8}$$

where f_0 is the Fermi distribution function at zero temperature. Since f_0 is a function of $(E–E_F)$, $G(E)$ in eq 8 leads to thermal smearing[16] of the conductance staircase expected from eq 1. The linear response is valid as long as the transmission function is independent of energy and is unaffected by the bias. Thus, if the bias is small, such that $\Delta\mu << \varepsilon_c$ + few k_BT, where ε_c is the energy range over which $T(E)$ can be assumed uniform (correlation energy), the expression for the current flowing from lead 1 to lead 2 can be linearized to give:

$$I_2 = G_{1\to2}(E)[V_2 - V_1] \tag{9}$$

The above discussion can be extended for multi-terminal measurements (Büttiker)[17] and is then referred to as the Landuer–Büttiker (LB) formalism. The LB formalism is valid as long as transport across the conductor is coherent, that is, only if the probe separation is much larger than l_ϕ. For non-coherent transport, it is still valid as long as the transport does not involve flow of electrons between different energy sub-bands (transverse modes). If this flow does exist, it can be neglected if the transmission functions are almost constant over the energy range where transport occurs.

Since a DTSTM is composed from two probes and a sample, an attempt to measure the resistance using the LB three-terminal device setup can be made. If the first tip is grounded, by applying a positive voltage on the sample (S) V_{s1} and a higher voltage on the second tip V_{21}, the surface resistance can be defined as $R_{21} = (V_{s1}/I_2)$.

Localization

In the LB formalism, electrons are treated as purely classical particles neglecting any quantum interference between successive scatterers. For a linear density of scatterers ν, having transmission probability of T each, and by defining $L_0 \equiv T/\nu(1–T)$, the transmission probability for a conductor of length L is given by $T(L)$ =

$L_0/(L + L_0)$. Substituting $T(L)$ into the resistance from eq 5, the linear growth with the length of any array of scatterers, as expected for "Ohmic" resistance, can then be recovered for large conductors with negligible contact resistance:

$$\rho(L) = (1/M)(1 - T(L))/T(L) = L/ML_0 \qquad (10)$$

In eq 10, ρ denotes the resistance, *normalized* to $(h/2e^2)$.But, when the dephasing length is much larger than the elastic mean free path $l_e << l_\phi$, the conductor can be viewed as a series of phase-coherent units. The electron transport in these units belongs to the regime of quantum diffusion (first introduced by Anderson[18] in 1958) where interference between different scatterers is present. By ensemble averaging over many units with different configuration of scatterers, a single-mode ($M = 1$) quantum resistor exhibits exponential increase above some L:

$$\rho(L) = 1/2[\exp(2L/L_0)–1] \qquad (11)$$

This non-"Ohmic" behavior can be deduced for the single-mode conductor,[19] and also for a multi-mode conductor[20] if L is long enough to have $\rho(L) \sim h/2e^2$. From (10) it is straightforward to see that for $M > 1$ it requires that L will exceed ML_0. The latter is known as the localization length $l_c = ML_0$.

Since $\rho(L)$ is *normalized* to $(h/2e^2)$, l_c is defined as the length above which the resistance is greater than $h/2e^2$. A conductor having phase-coherent segments with $l_\phi > l_c$ is said to be strongly localized. The resistance in this regime is subject to fluctuations, on several orders of magnitudes in scale, as a function of magnetic field or electron density. If, on the other hand, $l_\phi << l_c$ the conductor is *weakly localized*. In this regime, eq 11 can be expanded in a Taylor series replacing L_0 with l_c to give:

$$\rho(L) \sim [L/l_c + (L/l_c)^2] \qquad (12)$$

The first term in eq 12 is just the classical *normalized* resistance ρ_{CL} while the second represents the quantum deviation Δρ, which is proportional to the classical *normalized* resistance squared $\Delta\rho \propto \rho^2$. Therefore, for $l_\phi << l_c$, we get a constant correction to the conductance due to quantum interference:

$$\Delta G/(2e^2/h) = \Delta(1/\rho) = -\Delta\rho/\rho^2 \sim -1 \qquad (13)$$

Thus, for a macroscopic conductor in the *weak localization* regime, a quantum correction of the order of $\Delta G \sim -2e^2/h$ to the "Ohmic" conductance is expected. The reason for this reduction can be deduced if we replace the transmission probability in eq 4 with the reflection probability $R = 1 - T$. Given the classical formula $R(L) = L/(L + L_0)$ for $l_e << L$ and isotropic scatterers, the probability for mode m to be reflected into all modes ($n = 1, 2, \ldots, M$) is equal in the classical case,

$$R_{CL}(m \rightarrow n) = (1/M)[L/(L + L_0)]$$

When quantum interference is to be considered, the average result for $n \neq m$ is the same, but the perfect coherence between time-reversed paths leads to doubling of the probability for reflection into the incident mode $n = m$,

$$\langle R_Q(m \rightarrow n)\rangle = (1/M)[L/(L + L_0)] \text{ for } n \neq m$$
$$= (2/M)[L/(L + L_0)] \text{ for } n = m$$

This enhanced backscattering, associated with electromagnetic waves as well, has been observed directly[17] in 1986 and discussed theoretically[18] back in 1958. Thus, the average quantum reflection probability $\langle R_Q\rangle = \sum_n\langle R_Q(m \rightarrow n)\rangle$ has an extra term $(1/M)[L/(L + L_0)]$ added to it. For $\langle T_Q\rangle = 1–\langle R_Q\rangle$ the average transmission probability is $(1/M)[L/(L + L_0)]$ smaller than the classical value, and for $L >> L_0$,

$$\langle T_Q\rangle = T_{CL}–(1/M)[L/(L + L_0)] \approx T_{CL}–1/M$$

substituting $\langle T_Q\rangle$ into eq 3 gives:

$$\langle G_Q\rangle = (2e^2/h)M(T_{CL}–1/M) = G_{CL}–2e^2/h \qquad (14)$$

In the *weak localization* regime the quantum conductance depends on the scatterer's configuration and that also leads to fluctuations in the total reflection due to random interference. Fluctuations in G, of the order of $2e^2/h$, can thus be observed[19] in different mesoscopic samples. These are called *universal conductance fluctuations*.

Fluctuations can also arise from noise. Out of equilibrium, and at finite temperatures, the noise in two-terminal mesoscopic conductors contains the effect of both the thermal fluctuations in the incident electron beam as well as the partition noise due to the discrete nature of carriers. However, we do not expect to see this small signal in our measurements.

Mesoscopic Transport and Multi-Probe STM

For resistance measurements in large macroscopic conductors a multi-terminal Hall-bridge is commonly used. By applying current between two terminals, an additional two floating terminals can be placed in the current path and serve as voltage probes p_1 and p_2 that sense the electrochemical potential. Thus, G_s^{-1} can be found directly from $\Delta V/I$ with no contact resistance. For non-ballistic conductors, the electron number drops sharply, when they undergo a scattering process, due to the transmission probability T, thus forming a mesoscopic dipole. These "resistivity dipoles" produce local electric fields and contribute to the inhomogeneous nature of

conductors on the mesoscales. Hence, on these scales, when the voltage probes are fabricated across a scatterer, difficulties can arise in the application of eq 5. First, on these scales the probes might be the main source for scattering (and hence resistance). To minimize this perturbation, the probes have to be weakly coupled to the conductor; thus STM probes are good candidates. Second, the probes can be coupled differently to the electron states on each side, leading to a measured resistance value between a max. of G^{-1} and a min. of a reduced actual conductance, which is equal to $(h/2e^2M)(1–2T)/T$ (that can even be negative for T > 0.5). Third, unless the probes are located much further away from the scatterer than the dephasing length, quantum interference will strongly affect the measured potential drop. Thus, 4-probe measurements can be applied safely only if the conductor is coherent, that is, only if l_ϕ << probe separation d. Hence, by reducing d, a direct determination of the actual conductance, in the presence of scatterers, is no longer available. On the other hand, a DTSTM can collect the transconductance current between its probes; thus, the overall G can be found from $\partial I_2/\partial V_1$. If I scales linearly with ΔV, by changing d, the actual resistance can be found from the slope of G^{-1} vs d. The intersection will then give the contact resistance G_c^{-1}. We now move on to a compact review of the MPSTM achievements so far and our new concept.

A NEW CONCEPT FOR A DTSTM

MPSTM—Current Status

The experimental work in the field of multi-probe STM can be divided into two basic practices, micro four-point probe (μ-4pp) and dual-tip STM. In μ-4pp Hall-bridge measurements are performed with either fixed or 4 independent STM probes, and with linear or square probe arrangement. The fixed probes are silicon-fabricated "forks" like chips, with different probe separation, and they are brought into contact with a surface using a high-resolution scanning electron microscope (SEM). The 4 independent STM probes are standard STM tips mounted on 4 micromanipulators and they are also aligned under a SEM or CCD camera. So far, μ-4pp were able to show surface sensitivity versus probe spacing[5,21,22] anisotropic surface conductivity,[23] conductivity across an atomic step,[24] and the conductivity of nanowires[25] and nanotubes (NT).[26]

DTSTMs are more commonly built. Different designs were published,[27–41] all use standard STM tips, and their aligning is being performed either with special aligning-sample,[29] aligning-algorithm,[42] or again in SEM. So far, DTSTM accounted for overlapping images on sub-micron scales, three-terminal ballistic electron emission spectroscopy,[38] current–voltage curves of a single NT ring,[39] and conductivity of nanowires and nanotubes, also as a function of tip separation.[42]

Standard STM tips are usually electrochemically etched W wires, 125–250 microns in diameter. Hence, even for a small radius of curvature at the apex, approaching within a nano-gap separation with the two tips on the surface is impossible. High aspect ratio tips are needed and those can't be too long since they might bend due to the Van der Waals forces. Indeed, attempts to attach nanotubes or nanorods to the standard STM tips to reduce tip separation can be found,[39,41-44] but, no quantitative results were yet reported. In the following we introduce a new concept of a DTSTM based on the MCBJ with two EBID nanotips that can approach at nano-gap separation on the surface.

From a MCBJ to a DTSTM

The MCBJ[45–47] is a novel technique in which a notched-wire/thin-film/lithographically-designed junction, held at two close points on a bending beam, is being broken. By releasing the pressure (to bend), the two sides of the junction can then be tuned, with extreme precision and stability, to form atomic point contact. An extension of the MCBJ is what is sometimes called the MCB-STM.[48] Here a thin piece of piezo material, put between the wire and the bending beam, enables scanning the two electrodes one in front of the other. Unfortunately, the scanned surfaces are random and not much can be concluded from such measurements. In order to scan a desired sample, both sides of the junction have to simultaneously face a third surface (instead of each other), to be aligned in 3D, and must have scanning probe capabilities. To meet this challenge we developed a DTSTM based on the MCBJ with two fabricated EBID nanotips. We find the stability and alignment of the BJ to be a good starting point for a two-electrode system based on a "constant" nanogap separation. Our design is a modified version of the MCB-STM. But, unlike the traditional bending, which applies lateral force on the junction, in our design the breaking mechanism applies torque on a virtual pivot running through the junction. The breakage is then aligned with a two-tangential springs-hinge, which supplies the return force and insures that the two sides of the junction remain close although a small angle is applied (see Fig. 1d,f). The angle is necessary in order to enable tunneling of the tips when approaching with the sample. The junction consists of a Si wafer shaped by a double-sided anisotropic etching to form a 50-micron-wide bridge as a base for EBID tips (see Fig. 2). Nanotips with controlled architecture and from a variety of materials (see Fig. 3) are then fabricated on each side, using EBID techniques. The wafer

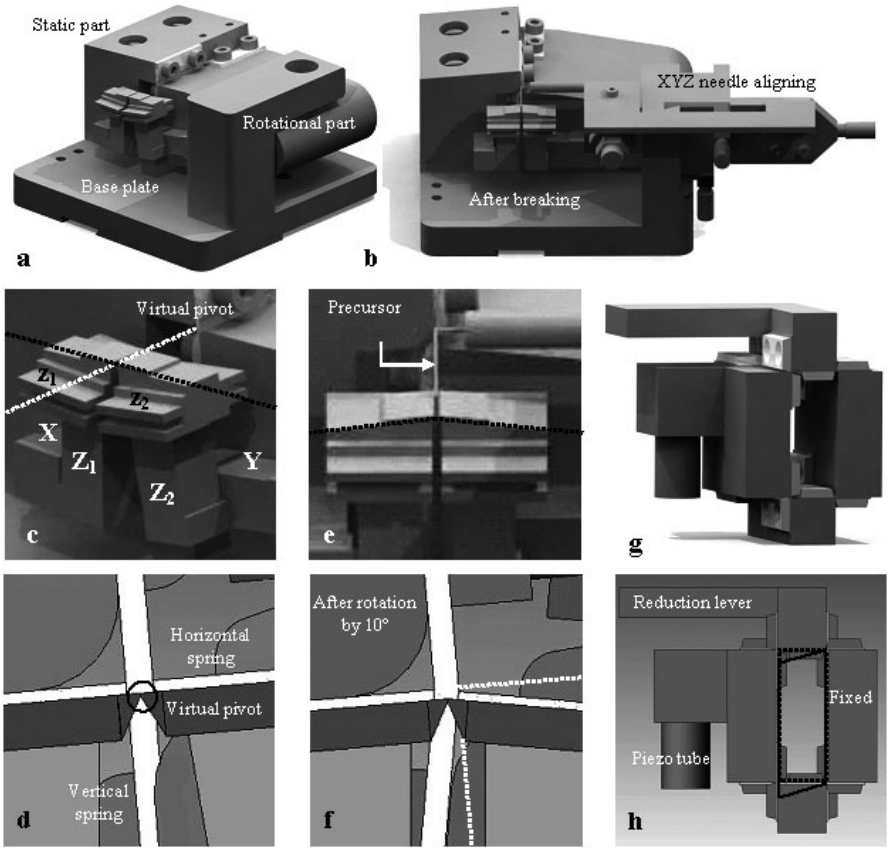

Fig. 1. The apparatus. (a) The BJ mechanism before breaking. The two prisms are aligned, as can be seen below in (c). (b) After breaking with the XYZ needle aligning kit. The two prisms are tilted 5° with respect to the horizon, as can be seen below in (e). (c) Before breaking—the virtual pivot is marked with a dotted white line. The dotted black line shows the junction aligning. Also labeled are the X, Y, and double Z aligning piezos and the "feedback" piezos. (d) The two-spring virtual hinge before breaking. (e) After breaking—the dotted black line shows the symmetric 5° tilt. (f) After the silicon is broken and the rotational part revolves by 10°, the spring-hinge keeps the junction at the revolution pivot. (g) The eight-spring four-hinge system for parallel sample approach. (h) When the lever is pushed down, the two right hinges are fixed and thus, a parallel deformation is formed as indicated in the transition from dotted black rectangle to full black parallelogram.

is glued on two XZ and YZ piezoceramics for XYZ aligning of the tips in 3D under the SEM before approaching to tunneling. Each side is also equipped with high-resolution, high-resonance frequency Z-piezo for independent tip oscillation controlled by its own separate feedback. The sample is mounted on a piezotube for XY scanning and tilt compensation. A piezo-motor will get the sample into tunneling with the higher tip while the second tip will later approach with its Z-piezo. The approach mechanism consists of an eight-spring four-hinge system for parallel confinement of the sample motion while the motor pushes a reduction lever on an arc path (see Fig. 1h). After both tips are in tunneling, the sample will scan in the XY surface while two separate feedbacks will simultaneously control the tip–sample distance. From the overlap of the two images, tip spacing and orientation with respect to the surface will be inferred. The XZ and YZ aligning piezos can then be used to relocate the tip, in order to perform the desired experiment.

Since the signals in mesoscopic transport measurements are small, tip stability (and corresponding current stability) is crucial. In order to collect meaningful data, mesoscopic transport experiments are frequently made at low temperatures. Thus, after the merit of our design will hopefully be demonstrated, by collecting two simultaneous STM images on a nanogap separation, a low-temperature version will be attempted.

Anisotropic Etching of Silicon BJ

Anisotropic wet etching on the front and back sides of a (100) silicon wafer is applied for the fabrication

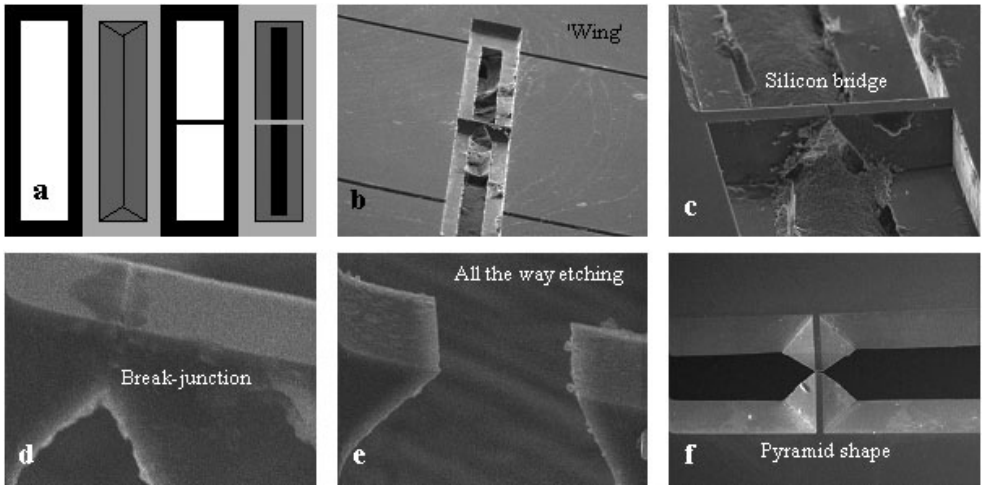

Fig. 2. The silicon break-junction. (a) (*left half*). The first (bottom) mask (white is open) and its V-grove pattern (gray is surface). (*right half*)—The second (top) mask and the final bridge over the trench. (b) SEM image of the anisotropic etch wafer. Seen is the bridge over the trench and additional grooves for breaking the wings after wafer attachment. (c) The silicon break-junction bridge. (d) Etching with finite junction width. (e) Etching through with a gap left. (f) A pyramid-shape junction.

of a silicon micro break-junction. Anisotropic etching is a chemical process in which the lateral etch rate can be much larger or smaller than the vertical etch rate, depending upon orientation of mask edge to crystalline axes. Our desired junction architecture can be fabricated in two etching processes (see Fig. 2a.). A low-stress SiN layer is deposited on both sides of the wafer. Cavities are then being patterned on one side with a first mask. The silicon is etched in a KOH solution, resulting in V-grooves. The PECVD SiN layer is applied to protect the grooves, and cavities are patterned on the other side of the wafer with a second mask. A second etching in KOH results in a 3D 50-micron-wide and 1-mm-long silicon break-junction.

EBID for SPM Probes Fabrication

Focused electron-beam-induced deposition and etching[49] are direct-write nanofabrication practices that enable selective deposition or removal of materials in 3D. Essentially, these processes are governed by an electron-induced reaction with a precursor vapor, which may either result in decomposition to a solid deposit or in formation of a volatile etch byproduct. In this relatively new field of interest, more and more scientific research is being conducted to understand, and hence improve, the modus operandi. This includes a better understanding of the underlying physics and chemistry, and better control over the process parameters such as precursor combinations and vapor pressure, target temperature, and e-beam energy and flux. In SPM, it is familiar mostly as a way to fabricate AFM nanoprobes at the apex of the traditional silicon pyramids.[50] Since H and C are always part of the deposit metrics, the fabrication of good conductive materials is more difficult, thus, EBID for making STM probes is so far not popular.

We fabricate EBID nanoprobes on both cantilevers formed by breaking the silicon bridge. Since the position, tilt, width, length, cone shape, and material can, to a certain degree of accuracy, be controlled, these are the ultimate candidates for DTSTM tips on a nanogap separation. The combination of high aspect ratio probes with a variety of materials can advance the DTSTM towards a more local (smaller probe separation), more versatile (for example, magnetic probes) data collection.

In the following section, our progress and preliminary results will be presented.

PRELIMINARY RESULTS

The Apparatus—(Fig. 1)

The dual-tip STM has two major sub-devices and two aligning kits. The devices are the BJ and the sample mechanisms, and the kits are the sample attachment and the EBID needle aligning.

The lower device is the break-junction complex. This complex includes a base plate with the BJ static part and a rotational part. XZ and YZ aligning piezo-stacks are attached to the static and rotational parts, respectively (Fig. 1c). On top of each side, a second Z-piezo (controlled by a separate feedback) is mounted with dielectric plates and a 5° prism. When the silicon is attached (using a special aligning kit) the upper part of the static prisms has 5° inclination with respect to the base

plate and the rotating prism is aligned with it (Fig. 1c). When torque is applied on the rotational side, the silicon breaks and the rotation stops after 10° at a symmetric 5° inclination of the second prism (Fig. 1e). The mutual inclination insures zero extent along the junction while the etched silicon gives a 50-micron width perpendicular to the junction. When tunneling with 2-nm tips, the junction spatial dimensions are critical to avoid crashing between the sample and silicon wafer. The junction keeps its position by two tangential spring-hinges. The spring-hinge manipulates a virtual pivot (extending through the junction) around which the rotational side revolves. In order to find the two sides of the broken silicon bridge at a few micron separation after the rotation, the desired junction has to be placed very accurately at the revolution pivot. A special aligning kit was developed in order to meet this demand.

By keeping the junction with a gap of microns, the road for the fabrication of two microprobes is open. Two inclining EBID tips, a few microns long and 100–200 nm wide, are now fabricated on both sides of the junction. An additional XYZ aligning kit with three axis micrometer screws can be mounted on the base plate with a special adaptor for precursor delivery.

The upper device is a bridge mounted on the base plate for sample approach and scanning. The approach mechanism includes an eight-spring four-hinge mechanism, a translational reduction-lever, and a piezo motor. The hinge system is organized in rectangular symmetry with one side fastened to the bridge, and the sample is mounted on the opposite side. When the motor pushes the lever, it revolves and torque is applied around the hinges. But, since one side (two hinges) can't move, the rotation of the lever (for small angles) turns into a parallel translation of the sample while the rectangle transforms to a parallelogram (Fig. 1h). Finally, the sample is mounted on a piezo-tube for scanning and tilt compensation.

The DTSTM experiment is performed in a high-vacuum chamber on a custom-made damping system. The system consists of three stages; spring suspension, Eddy-current, and Viton rings.

The Silicon Break-Junction—(Fig. 2)

In the anisotropic etching process a total of 54 junction-chips are fabricated on one 4″ silicon wafer. Every chip consists of one 50-micron by 1-mm bridge over a trench 1 mm wide and 5 mm long, with two protection "wings" at the sides (Fig. 2b). After the wafer is glued with the sample attachment kit, the wings are broken with a small guillotine and the bridge is left on its own (Fig. 2c). The etching process can be stopped, leaving a 30–50 micron width at the breaking point, or it can be continued all the way leaving a small gap (Fig. 2e,d). In the first option, the junction can be broken and a cut with rigid cantilevers for the tip fabrication is formed. The disadvantage lies in the possibility of keeping the junction close (due to the angle applied by the breaking mechanism) without probable risk of crashing. The second option results in a "zero" width two-prism junction. The junction here can be brought to "zero" proximity at the price of fragility. Another design can result with a pyramid-shape junction (Fig. 2f).

At the end of the process, the wafer is covered with gold for improving the contact to the external electrodes and to prevent the metal molecules applied by EBID from diffusing into the silicon.

EBID Fabrication—(Fig. 3)

The fabrication of EBID nanotips is done inside an IC845 SEM by JEOL equipped with an ELPHY PLUS electron beam lithography system by RAITH. Two kinds of nanotips were fabricated. The first is carbon-based and fabricated after applying a small drop of paraffin oil on the silicon surface and radiating to the desired location with the electron beam using spot mode. These nanotips are easier to reproduce but they are too soft for STM applications and their conductance quality can't be guaranteed. An E-beam evaporation system by TECTRA for W coating was installed in the vacuum chamber to solve these problems. The second kind of nanotip is Rh-based and it is fabricated[51] by application of $[RhCl(PF_3)_2]_2$. Here the solid metalorganic molecules are stored in a small reservoir and delivered within 50-micron proximity to the fabrication site by a needle with a 500-micron inner diameter. The aligning is done with an XYZ mini manipulator mounted with an adaptor on the base plate of the apparatus, before the introduction of the breaking mechanism into the SEM (Fig. 1b). The tips were grown with different beam diameter, accelerating voltage, current, and for variable deposition times. The following features could be accomplished: (1) The site of the fabrication can be selected with 10-nm precision. (2) The diameter and length of the tips can be controlled by the beam diameter and fabrication time, respectively. Tips can be grown up to a few microns long with down to 100-nm width. (3) The tilt of the tips can be controlled with the SEM stage for mutual inclination. (4) The tip apex can be rounded or sharp. A sharp cone enables one to approach with two inclining tips much closer than their diameter. The tips can be brought to their minimum separation when the inclination equals their cone angle. (5) Different tip shapes can be fabricated for a versatile 3D approach to the surface and differential strength (a tip can have a strong base and small sensor at its apex). (6) A bridge can be grown across the

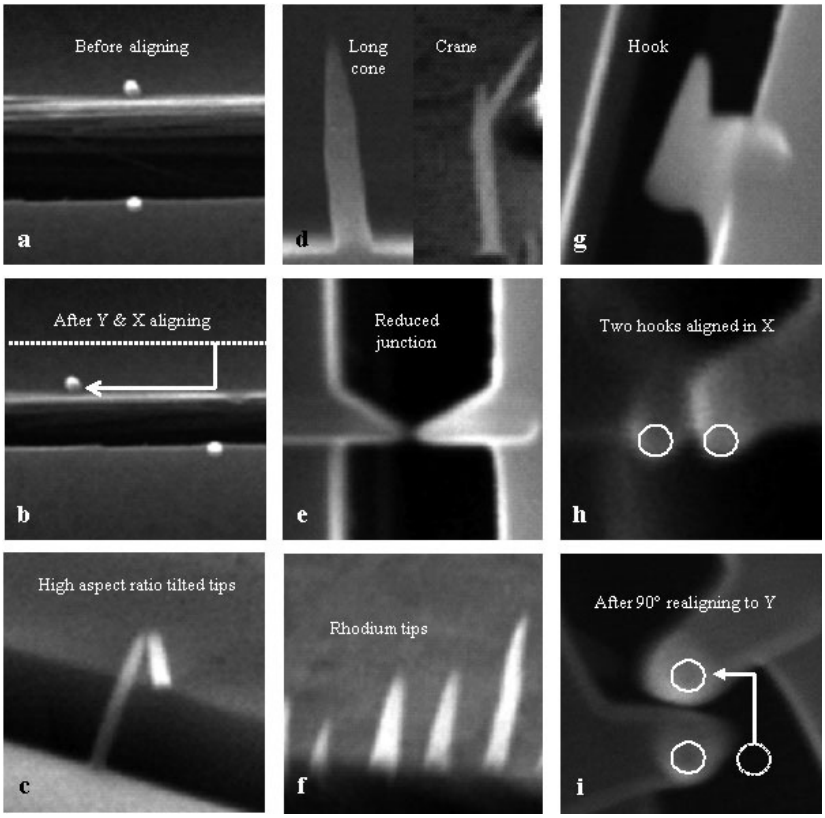

Fig. 3. EBID tips. (a) Two tips fabricated on both sides of the broken silicon. (b) After aligning in X and Y, as indicated by the white arrow. (c) When the tips are tilted, the gap can be closed and the tips (here ~2.5 microns long and ~200 nm wide) can be brought within a proximity of less than 100 nm. (d) Vertical orientation, with long cone and "crane"-shape tips. (e) Reduced junction by two fabricated cantilevers. (f) Rhodium tips. (g) A "Hook-like" tip after working in line mode follows by spot mode. (h) Two "hook-like" tips. (i) After realigning, a 90° change of the tip apex orientation is achieved (as indicated by the white

junction to close its gap and serve as a new reduced-dimension junction. (7) Using the XZ, XY piezos, the junction, hence, the tips could be aligned with different separation and orientation.

CONCLUSIONS

The relations between the conductor's dimensions and its characteristic length scales affect the electron transport properties. By reducing the probe separation in DTSTM, physical phenomena typical of smaller dimensions, especially at finite temperatures, can be more accessible. Our design is capable of reducing probe spacing below 100 nm, and thus has a potential to reveal more local properties of the electron transport on surfaces.

Acknowledgments. This work was supported by a grants from the Israel Academy of Sciences (ISF), the Israeli Ministry of Sciences for binational collaboration between Korea and Israel, and the Wolfsohn Foundation.

REFERENCES AND NOTES

(1) Heike, S.; Watanabe, S.; Wada, Y.; Hashizume, T. *Phys. Rev. Lett*. **1998**, *81*, 890.
(2) Hasegawa, Y.; Lyo, I.-W.; Avouris, Ph. *Surf. Sci*. **1996**, *357*, 32.
(3) Himpsel, F.J. *Adv. Phys*. **1983**, *32*, 1.
(4) Kaiser, W.J.; Bell, L.D. *Phys. Rev. Lett*. **1988**, *60*, 1406.
(5) Hasegawa, S.; Shiraki, I.; Tanabe, F.; Hobara, R.; Kanagawa, T.; Tanikawa, T.; Matsuda, I.; Petersen, C.L.; Hansen, T.M.; Boggild, P.; Grey, F. *Surf. Rev. Lett*. **2003**, *10*, 963.
(6) Data, S. *Electron Transport in Mesoscopic Systems*; Cambridge University Press: Cambridge, 2001.
(7) Mello, P.A.; Kumar, N. *Quantum Transport in Mesoscopic Systems*; Oxford University Press: New York, 2001.
(8) Niu, Q.; Chang, M.C.; Shih, C.K. *Phys. Rev. B* **1995**, *51*, 5502.
(9) Imry, J. *Physics of Mesoscopic Systems*; World Scientific Press, Singapore: 1986.
(10) Engquist, H L.; Anderson, P.W. *Phys. Rev. B* **1981**, *24*, 1151.

(11) Sharvin, Yu.V.; Bogatina, N.I. *Sov. Phys. JETP*, **1969**, *29*, 419.

(12) van Wees, B.J.; van Houten, H.; Beenakker, C.W.J.; Williamson, J.G.; Kouwenhoven, L.P.; van der Marel, D.; Foxon, C.T. *Phys. Rev. Lett.* **1988**, *60*, 848.

(13) Wharam, D.A.; Thornton, T.J.; Newbury, R.; Pepper, M.; Ahmed, H.; Frost, J.E.F.; Hasko, D.G.; Peacock, D.C.; Ritchie, D.A.; Jones, D.A.C. *J. Phys. C* **1988**, *21*, L209.

(14) Topinka, M.A.; LeRoy, B.J.; Shaw, S.E.J.; Heller, E.J.; Westervelt, R.M.; Maranowski, K.D.; Gossard, A.C. *Science* **2000**, *289*, 29.

(15) Landauer, R. *IBM J. Res. Dev.* **1988**, *32*, 306. Landauer, R. *Phys. Scripta* **1992**, *T42*, 110.

(16) Kristensen, A.; Bo Jensen, J.; Zaffalon, M.; Sørensen, C.B.; Reimann, S.M.; Lindelof, P.E.; Michel, M.; Forchel, A. *J. Appl. Phys.* **1998**, *83(1)*, 607.

(17) Büttiker M. *J. Res. Dev.* **1988**, *32*, 317.

(18) Anderson, P.W. *Phys. Rev.* **1958**, *109*, 1492.

(19) Landauer, R. *Philos. Mag.* **1970**, *21*, 863.

(20) Thouless, D.J. *Phys. Rev. Lett.* **1977**, *39*, 1167.

(21) Shiraki, I.; Tanabe, F.; Hobara, R.; Nagao, T.; Hasegawa, S. *Surf. Sci.* **2001**, *493*, 643.

(22) Hasegawa, S.; Shiraki, I.; Tanikawa, T.; Petersen, C.L.; Hansen, T.M.; Boggild, P.; Grey, F. *J. Phys.: Condens. Matter* **2002**, *14*, 8379.

(23) Kanagawa, T.; Hobara, R.; Matsuda, I.; Tanikawa, T.; Natori, A.; Hasegawa, S. *Phys. Rev. Lett.* **2003**, *91*, 036805.

(24) Matsuda, I.; Ueno, M.; Hirahara, T.; Hobara, R.; Morikawa, H.; Hasegawa, S. *Phys. Rev. Lett.* **2004**, *93*, 236801.

(25) Okino, H.; Matsuda, I.; Hobara, R.; Hosomura, Y.; Hasegawa, S.; P. Bennett A. *Appl. Phys. Lett.* **2005**, *86*, 233108.

(26) Hobara, R.; Yoshimoto, S.; Ikuno, T.; Katayama, M.; Yamauchi, N.; Wongwiriyapan, W.; Honda, S.; Matsuda, I.; Hasegawa, S.; Oura, K. *Jpn. J. Appl. Phys.* **2004**, *43*, L1081.

(27) Tsukamoto, S.; Siu, B.; Nakagiri, N. *Rev. Sci. Instrum.* **1991**, *62*, 1767.

(28) Aono, M.; Jiang, C.-S.; Nakayama, T.; Okuda, T.; Qiao, S.; Sakurai, M.; Thirstrup, C.; Wu, Z.-H. *J. Surf. Sci. Soc. Jpn.* **1998**, *19*, 698 (in Japanese).

(29) Okamoto, H.; Chen, D.M. *Rev. Sci. Instrum.* **2001**, *72*, 4398.

(30) Grube, H.; Harrison, B.C.; Jia, J.; Boland, J.J. *Rev. Sci. Instr.* **2001**, *72*, 4388; *Rev. Sci. Instrum.* **2002**, *73*, 1343.

(31) Watanabe, H.; Manabe, C.; Shigematsu, T.; Shimizu, M. *Appl. Phys. Lett.* **2001**, *78*, 2928; **2001**, *79*, 2462.

(32) Takami, K.; Akai-Kasaya, M.; Saito, A.; Aono, M.; Kuwahara, Y. *Jpn. J. Appl. Phys.* **2005**, *44*, L120.

(33) Ishikawa, M.; Yoshimura, M.; Ueda, K. *Jpn. J. Appl. Phys.* **2005**, *44*, 1502.

(34) Xu, J.F.; Thibado, P.M.; Ding, Z. *Rev. Sci. Instrum.* **2006**, *77*, 093703.

(35) Wu, W.; Guha, A.; Kim, S.; de Lozanne, A. *IEEE Transact. Nanotechnology* **2006**, *2*, 5.

(36) Cai, W.; Pang, F.; Wang, J.; Liu, H.; Liang, X.J.; Xue, Q.K.; Chen, D.M. *Rev. Sci. Instrum.* **2007**, *78*, 065108.

(37) Jaschinsky, P.; Coenen, P.; Pirug, G.; Voigtländer, B. *Rev. Sci. Instrum.* **2006**, *77*, 093701.

(38) Kaya, Yi, I. I.; Altfeder, I.B.; Appelbaum, I.; Chen, D.M.; Narayanamurti, V. *Rev. Sci. Instrum.* **2005**, *76*, 063711.

(39) Watanabe, H.; Manabe, C.; Shigematsu, T.; Shimizu, M. *Appl. Phys. Lett.* **2001**, *78*, 2928.

(40) Grube, H.; Harrison, B.C.; Jia, J.; Boland, J.J. *Rev. Sci. Instrum.* **2001**, *72*, 4388.

(41) Takami, K.; Akai-Kasaya, M.; Saito, A.; Aono, M.; Kuwahara, Y. *Jpn. J. Appl. Phys.* **2005**, *44*, L120.

(42) Shingaya, Y.; Nakayama, T. NIMS NOW **2004**, *2*, 1,3.

(43) Murata, Y.; Yoshimoto, S.; Kishida, M.; Maeda, D.; Yasuda, T.; Ikuno, T.; Honda, S.; Okado, H.; Hobara, R.; Matsuda, I.; Hasegawa, S.; Oura, K.; Katayama, M. *Jpn. J. Appl. Phys.* **2005**, *44*, No. 7B, 5336.

(44) Shingaya, Y.; Nakayama, T.; Aono, M. *Physica B* **2002**, *323*, 153.

(45) Moreland, J.; Etkin, J.W. *J. Appl. Phys.* **1985**, *58*, 3888.

(46) Muller, C.J.; Van Ruitenbeek, J.M.; de Jong, L.J. *Phys. Rev. Lett.* **1992**, *69*, 140.

(47) Van Ruitenbeek, J.M.; Alvarez, A.; Piñeyro, I.; Grahmann, C.; Joyez, P.; Devoret, M.H.; Esteve, D.; Urbina, C. *Rev. Sci. Instrum.* **1996**, *67*, 108.

(48) Keijsers, R. Ph.D. Thesis, University of Nijmegen, 1998.

(49) Rack, P.D.; Randolph, S.; Deng, Y.; Fowlkes, J.; Choi, Y.; Joy, D.C. *Appl. Phys. Lett.* **2003**, *82*, 2326.

(50) Hafner, H.; Cheung, C.L.; Woolley, A.T.; Lieber, C.M. *Prog. BioPhys. Mol. Biol.* **2001**, *77*, 73.

(51) The precursor is supplied by Phong Dinh Tran and Pascal Doppelt.